Article

Improved Tribological Performance of Nitride-Reinforced Biocompatible Titanium–Niobium–Zirconium–Tantalum (TNZT) Alloys for Advanced Orthopedic Applications

Satyavan Digole [1], Jay Desai [1], Calvin Christopher [1], Smriti Bohara [2], Chathuranga Sandamal Witharamage [3], Chandra Kothapalli [2], Rajeev Kumar Gupta [3] and Tushar Borkar [1,*]

[1] Department of Mechanical Engineering, Cleveland State University, Cleveland, OH 44115, USA
[2] Department of Chemical and Biomedical Engineering, Cleveland State University, Cleveland, OH 44115, USA
[3] Department of Materials Science and Engineering, North Carolina State University, Raleigh, NC 27695, USA
[*] Correspondence: t.borkar@csuohio.edu

Abstract: β-titanium (β-Ti) alloys are used in various biomedical applications, especially for orthopedic implants, due to their superior biocompatibility, excellent corrosion resistance, and enhanced mechanical properties. However, the inferior tribological properties of β-Ti alloys lead to fretting wear and a strong tendency to seize, which is a major concern in orthopedic applications involving continuous friction. This work aims to address this issue by incorporating biocompatible nitrides in Ti-Nb-Zr-Ta (TNZT) β-Ti alloys. TNZT composites comprising 2 wt.% of biocompatible nitrides (TiN, NbN, ZrN, and TaN) were prepared using high-energy ball milling followed by spark plasma sintering. All the nitrides improved the hardness and wear resistance of TNZT alloys and showed excellent biocompatibility. TNZT-2 wt.% TiN showed the average highest hardness of 311.8 HV and the lowest coefficient of friction of 0.659, suggesting the highest efficiency of TiN in improving the tribological performance of TNZT alloys. The underlying mechanisms behind the superior performance of nitride-reinforced TNZT composites are discussed in detail. The effect of TiN concentration was also studied by preparing TNZT composites with 5 and 10 wt.% TiN, which showcased a higher hardness of 388.5 HV and 444.3 HV, respectively. This work will aid in producing superior β-Ti alloys for advanced orthopedic applications.

Keywords: TNZT alloys; microstructure; nitrides; wear resistance; biocompatibility

1. Introduction

Recent advancements in the design of modern orthopedic implants have been greatly enhanced by the development of composite materials [1]. Several metallic, ceramic, and polymer-based composite biomaterials have been developed by researchers for various orthopedic applications [2–6]. About 80% of orthopedic implants are metal-based due to their excellent biocompatibility and superior mechanical properties. Metallic biomaterials are also remarkably important for reconstructing failed tissues [7]. Amongst all metallic biomaterials, titanium (Ti) and its alloys, mainly Ti-6Al-4V alloys, are the most widely used materials for orthopedic applications due to their excellent biocompatibility and corrosion resistance [8–10]. However, commercially used Ti alloys have a higher elastic modulus (110 ± 10 GPa) than human bones (10–40 GPa) [11,12]. The higher Young's modulus of metallic biomaterials compared with bone can lead to bone atrophy and stress shielding in joints, leading to the failure of an implant [13,14]. In order to improve the fatigue strength and wear resistance of metallic biomaterials, different types of reinforcements are added to the metal matrix [15–17].

The popularly known β-phase metastable Ti alloys, particularly Ti-Nb-Zr-Ta (TNZT), were developed to overcome stress-related failures by offering a lower Young's modulus than Ti-6Al-4V [18,19]. Additionally, the complicated flowing environment inside the body,

influenced by blood, proteins, and mechanical stress, encourages the release of alloying elements such as V, Ni, and Al, leading to allergic reactions and major long-term health issues, which can be overcome in these TNZT alloys [20–23]. With an elastic modulus of 50–65 GPa, which is closer to that of human bone, enhanced properties such as increased corrosion resistance, improved biocompatibility, better ductility, and formability compared to other variants of Ti alloys make β-Ti alloys suitable over other materials for orthopedic implants [7]. Although β-Ti alloys exhibit excellent biocompatibility and mechanical properties compared to traditional Ti alloys, they exhibit inferior tribological behavior, leading to wear (adhesion) failure and fretting fatigue [24–26]. To use β-titanium alloys (e.g., TNZT) for load-bearing orthopedic applications, the material should have a high abrasion resistance to minimize debris formation due to dynamic body movements [27,28]. Therefore, there is a critical need to improve the wear behavior of these β-Ti alloys. Several methods such as thermal spraying, laser treatment, ion implantation, plasma nitriding, physical vapor deposition (PVD), and laser gas nitriding, to name a few, are being used for the same purpose [29–32].

Based on recent research, ceramic-reinforced metal matrix composites (MMCs) exhibit promising results in terms of fracture toughness, wear resistance, and the mechanical strength of the alloy [33,34]. These MMCs offer enhanced interfacial bonding between the reinforcement and matrix. Typically, these reinforced particles are distributed uniformly within the matrix, resulting in better mechanical properties. Using this approach, a variety of matrix materials (Al, Ti, Cu, Ni, and Fe) and second-phase particles (borides, carbides, nitrides, and oxides) have been produced [35,36]. Therefore, reinforcing second-phase particles with a β-Ti alloy can potentially improve the tribological properties of the alloy in terms of wear and fretting fatigue. Composites reinforced with ex situ second-phase particles can be produced by different methods. Mechanical alloying (MA) is a solid-state powder processing method that involves the repeated cold welding and fracture of particles to produce various metallic alloys and composites [37,38]. This method can produce fine-grained alloyed powder particles in metal–metal and metal–ceramic systems [39,40]. In recent years, MA has been extensively used to fabricate ex situ particle-reinforced MMCs [41].

Spark plasma sintering (SPS) is an advanced processing technique that sinters mechanically alloyed metallic and composite powders. The SPS of ball-milled powders allows the fabrication of bulk materials from powders through a fast heating rate and short holding times at low sintering temperatures. This method is opted due to its efficiency and short processing time compared with traditional manufacturing methods for processing metallic alloys, such as hot isostatic pressing (HIP) and vacuum arc melting (VAM) [42]. Therefore, reinforcing biocompatible nitrides in the TNZT matrix through MA followed by the SPS process can result in modified wear properties. The main purpose of selecting nitride-based reinforcement is to increase the surface hardness of the material, its wear resistance, fatigue life, and corrosion resistance.

In this article, TNZT alloys have been reinforced with biocompatible nitrides (TiN, NbN, ZrN, and TaN) using MA followed by SPS processing. This study aims to investigate the effect of nitrides on microstructure, mechanical and tribological behavior, and the biocompatibility of nitride-reinforced TNZT composites.

2. Materials and Methods

2.1. Material Synthesis and Characterization

The prealloyed TNZT powder with a chemical composition of 53 wt.% Ti, 35 wt.% Nb, 7 wt.% Zr, and 5 wt.% Ta, with a purity of 99.9%, was procured from Tosoh SMD, Inc. (Grove City, OH, USA). Two sets of powdered samples were prepared. The first set consisted of a 2 wt.% of each nitride (TiN, NbN, ZrN, and TaN) mixed with TNZT powder. The second set contained a 5 wt.% and 10 wt.% of TiN mixed with TNZT powder.

The powder mixtures were ball milled using a Planetary mill PULVERISETTE 7 (FRITSCH, Idar-Oberstein, Germany). The ball-to-powder ratio (BPR) was maintained at

10:1 with the addition of 1 to 2 wt.% stearic acid (Sigma Aldrich, St. Louis, MO, USA) to prevent the cold welding of the alloy mixture during the mechanical alloying process. The mixture was mechanically alloyed for 1 h with a rotational speed of 200 rpm.

The mechanically alloyed powders were compacted into a bulk shape using an SPS 10–3 furnace by Thermal Technologies LLC (Santa Rosa, CA, USA). All samples were sintered at a temperature of 1100 °C for 5 min with a heating rate of 100 °C/min. This process was carried out under a controlled argon atmosphere to prevent any oxidation, while a pressure of 65 MPa was maintained throughout the sintering process. The final sample after SPS consolidation was in the form of a thin disc with a 20 mm diameter and 2.5 mm thickness.

The bulk densities of samples were determined using Archimedes' principle with DI water as the working medium. Relative density was calculated from the ratio of bulk density to theoretical density. The sintered samples were mounted using an ALLIED TechPress 3™ Mounting Press (Allied High Tech Products, Inc., Cerritos, CA, USA). The samples were polished with SiC abrasive paper (from grit size 240 to 1200) using a BUEHLER AutoMet™ 250 Grinder-Polisher (Beuhler, Lake Bluff, IL, USA)and then sonicated using ethanol for 10 min to remove any residual SiC that embedded itself in the samples while polishing. These polished samples were characterized by SEM/EDS using Inspect F50 (FEI now Thermo Fisher Scientific, Hillsboro, OR, USA). An electron backscatter diffraction analysis was performed to examine the crystalline orientation of the processed structure. The sintered, nitrided TNZT samples were subjected to X-ray diffraction (XRD), which was performed using a Rigaku Ultima III X-ray diffractometer (Rigaku Americas Corporation, Chapel Hill, NC, USA) with Cu Kα (λ = 1.54 Å). The EDS and XRD analyses were conducted to analyze the different phases present in the sintered sample. The microhardness was measured using a Microhardness Tester (Wilson VH1202 BUEHLER, Lake Bluff, IL, USA) under a load of 1.96 N for 15 s, with the average of 10 readings considered. Wear behavior was determined using a ball-on-disc tribometer. Wear tests on the alloy samples were conducted against a silicon nitride (Si_3N_4) ball of a diameter of 3 mm under a normal load of 1 N. The Si_3N_4 ball was used because of its high hardness and chemical stability. The sliding speed was set to 1260 mm/min with a radius of 2 mm for a total sliding distance of 200 m.

2.2. Biocompatibility Tests of the Alloys

2.2.1. Materials

Human MG-63 (CRL-1427) cells and an MTT cell proliferation assay kit were purchased from the American Type Culture Collection (Manassas, VA, USA). Cell culture materials including low-glucose Dulbecco's Modified Eagle Medium (Billerica, MA, USA), heat-inactivated fetal bovine serum (FBS; Gibco), penicillin/streptomycin (Gibco), 0.05% Trypsin-EDTA (Gibco), Hank's Balance Salt Solution (HBSS), and cell culture flasks were purchased from Thermo Fisher Scientific (Waltham, MA, USA). A Live/Dead viability/Cytotoxicity Assay Kit was purchased from Millipore Sigma (Billerica, MA, USA). An inverted fluorescence microscope (ZEISS Axio Vert.A1) (Dublin, CA, USA) and a Biotek Synergy H1Hybrid Multi-Mode microplate reader (Santa Clara, CA, USA) were used to obtain images and analyze samples, respectively. A Wilson VH 1202 micro hardness tester machine was used to determine the cellular adhesion on metal samples.

2.2.2. MG-63 Cell Culture

Human MG-63 cells (14-year-old, Caucasian, male, patient with osteosarcoma) were seeded in T-75 cell culture flasks using L-DMEM supplemented with 10% FBS and 1% penicillin/streptomycin and maintained at 37 °C in 95% humidity and 5% CO_2 incubators. After passaging, cells were seeded on metal discs placed in 12-well culture plates at a density of 38,000 cells/well. Four different alloy compositions were tested, with *n* = 4 discs/alloy type. The alloy discs were placed in separate wells in a 12-well plate, and 200 μL of cell suspension and 500 μL of complete medium were added to the surface of each alloy surface.

The samples were then placed in an incubator for 2 h to facilitate cell attachment. Then, 1.5 mL of additional complete media was added to each well. For the live/dead cell toxicity assay and the MTT colorimetric assay, the cells were grown for 48 h and 96 h, respectively.

2.2.3. Cell Viability Test

MG-63 cell viability was tested using a Live/Dead® assay kit from Millipore Sigma (Billerica, MA, USA) to determine the biocompatibility of alloys after 48 h exposure. Cells were stained with calcein-AM and ethidium homodimer solutions (37 °C, 1 h), washed with 1× PBS twice, and imaged using an inverted fluorescence microscope. Cells cultured directly on the plastic surfaces with no alloy discs served as controls.

2.2.4. MTT Assay

MG-63 cells were seeded on the alloy surfaces, at a density of 38,000 cells per well, in 12-well plates, and cultured for 96 h at 37 °C, 95% relative humidity, and 5% CO_2 levels. Then, 0.2 mL of MTT reagent was added to each well and incubated for 1 h. Upon a clearly visible purple precipitation, 0.2 mL of detergent reagent was added to each well. The plates were incubated for 1 h at 37 °C, and the absorbance was measured at a wavelength of 570 nm in a microplate reader. Cells cultured directly on the plastic surfaces with no alloy discs served as controls.

2.2.5. Cell Adhesion

The adhesion of MG-63 cells was analyzed using a Wilson VH1202 Micro Hardness Tester microscope (Lake Bluff, IL, USA). Cells were cultured on the surface of alloy samples for 48 h, washed with 1× PBS, fixed with 4% paraformaldehyde for 1 h, and washed again with PBS. The metal surfaces were imaged using a microhardness tester. Cells cultured directly on the plastic surfaces with no alloy discs served as controls.

3. Results

3.1. X-ray Diffraction

The XRD patterns of sintered pure TNZT alloy and TNZT composites with 2 wt.% of TiN, NbN, ZrN, and TaN are shown in Figure 1. Strong peaks at ~38.39°, ~55.53°, and ~69.60° indicate the firm presence of atoms in the (110), (200), and (211) planes, respectively, suggesting a single-phase BCC β-Ti phase. This phase is associated with the lower elastic modulus in Ti alloys required for ensuring superior biocompatibility and an appropriate environment for the growth of tissues near implants. The (110) plane showed the highest intensity, suggesting the preferred tendency of atoms to reside in this plane due to its association with a lower Gibbs free energy and stable atomic arrangement. No peaks of the HCP α-phase were observed due to the large amounts of β-stabilizing alloying elements (Ta and Nb). Ta and Nb promote the lowering of β-transformation temperature and aid in stabilizing β microstructure. The relatively higher XRD peak intensities of the (110), (200), and (211) planes of TNZT composites reinforced with TaN and NbN are in strong agreement with the same. The (211)/(200) intensity ratio is close to 1 for the pure TNZT alloy and TNZT-ZrN composite. This ratio increases to ~1.5 for TNZT–TaN and TNZT–NbN composites and ~2.2 for TNZT–TiN composites. The ratio of the highest (110) peak with other peaks showed no significant change in all the samples. The lattice parameters of all the samples were in close approximation to that reported for the β-Ti alloy (~3.3 Å). The XRD patterns of the nitride-reinforced TNZT composites do not show peaks associated with corresponding nitrides, primarily due to their low wt.% in these composites. Also, the addition of these nitride reinforcements did not affect the crystal structure or phase formation in these TNZT composites.
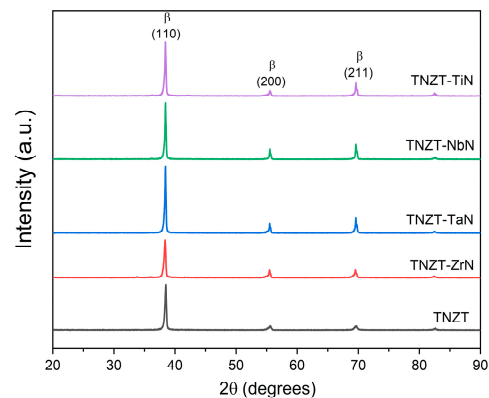
Figure 1. XRD of sintered pure TNZT alloy and nitride TNZT composites revealing a single β-phase (BCC) structure.

3.2. Scanning Electron Microscopy

The SEM images of the SPS-processed pure TNZT alloy and nitride-reinforced TNZT composites are shown in Figure 2. The pure TNZT alloy showed no evidence of compositional inhomogeneity, suggesting one dominant phase (β-Ti). No secondary phases were detected in this sintered alloy. The microstructures of TNZT-NbN, TNZT-TaN, and TNZT-ZrN composites also showed a dominant β-Ti phase (Figure 2c–h).

The SEM microstructures are in good agreement with the density measurements showing high densification (over 99%) and no significant porosity. The bright spots in all the SEM images are Ta-rich regions on the TNZT surface [43], as Ta being the heavier element appears bright in the backscattered images. Dark spots correspond to the presence of nitrides which are distributed throughout the β matrix. The SEM images depict that the grains are polyhedral and equiaxed with fine dark phases segregating at the grain boundaries for the nitrided TNZT composites. The grain-size analysis was performed by using ImageJ version 1.54h software to identify the effect of nitride reinforcement on grain size. Overall, 50 grains were considered to predict the average grain size of the sample. The measured grain sizes for pure TNZT, TNZT–NbN, TNZT–TaN, and TNZT–ZrN were 60.79 µm, 58.07 µm, 32.03 µm, and 34.03 µm. A lower grain refinement was observed for the TNZT–NbN composites, mainly due to the agglomeration of NbN within the TNZT matrix. The addition of TaN and ZrN shows a significant grain refinement, mainly due to the uniform distribution of these nitrides along the grain boundaries with less agglomeration, which is shown in Figure 2e,f and Figure 2g,h, respectively. The presence of nitride reinforcement prevents grain development and creates nucleation sites for new TNZT grains to grow during the recrystallization process, leading to grain refinement inside the TNZT matrix. A similar grain refinement was reported due to the reinforcement of TiB in the TNZT matrix [44].

Figure 3 shows the microstructure of the TNZT–TiN composites with 2 wt.% TiN, 5 wt.% TiN, and 10 wt.% TiN. The size and location of black spots in the TNZT–TiN composites with 5 wt.% TiN and 10 wt.% TiN suggest the higher segregation and nonuniform distribution of nitrides in the β-Ti matrix. In comparison with the 2 wt.% reinforcement of other nitrides (NbN, TaN, and ZrN), the 2 wt.% TiN shows the highest grain refinement with a grain size of 30.80 µm. Further, an increase in TiN reinforcement to 5 wt.% and 10 wt.% results in a further grain-size reduction to 20.28 µm and 16.78 µm, respectively.

The EDS map of TNZT-2 wt.% TiN composites showcasing the distribution of Ti and N is shown in Figure 4. It can be observed that the dark regions are TiN-rich regions, whereas the bright regions comprise Ti, Zr, Nb, and Ta distributed uniformly throughout the matrix.
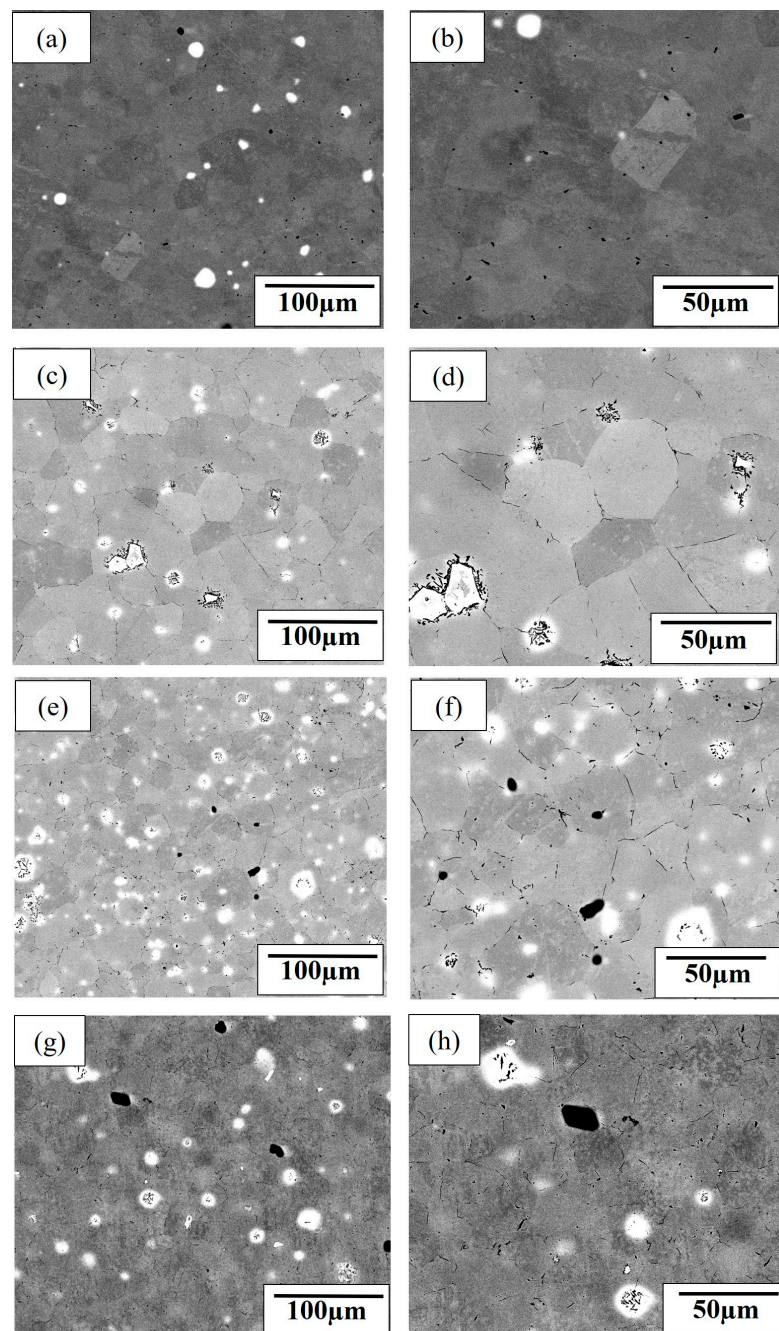
Figure 2. SEM backscattered images showing the microstructures of sintered TNZT alloys for (**a,b**) the pure TNZT alloy at (**a**) low magnification and (**b**) high magnification; (**c,d**) TNZT-2 wt.% NbN at (**c**) low magnification and (**d**) high magnification; (**e,f**) TNZT-2 wt.%TaN at (**e**) low magnification and (**f**) high magnification; and (**g,h**) TNZT-2 wt.% ZrN at (**g**) low magnification and (**h**) high magnification.
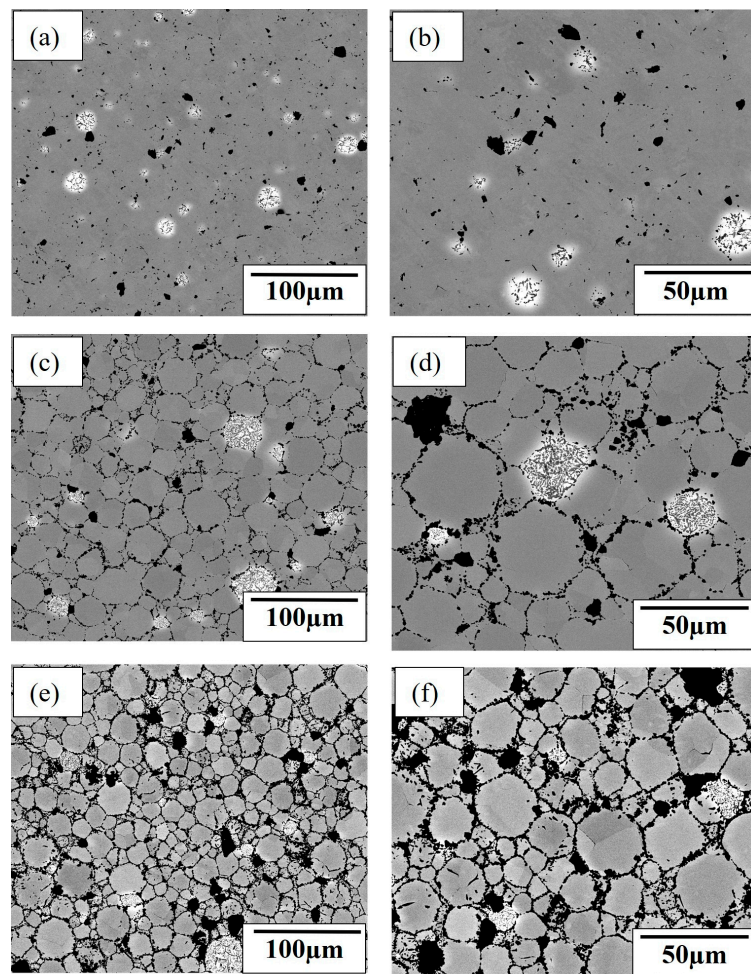
Figure 3. SEM backscattered images showing the microstructures of sintered TNZT alloys for (**a**,**b**) TNZT-2 wt.% TiN at (**a**) low magnification and (**b**) high magnification; (**c**,**d**) TNZT-5 wt.% TiN at (**c**) low magnification and (**d**) high magnification; and (**e**,**f**) TNZT-10 wt.%TiN at (**e**) low magnification and (**f**) high magnification.
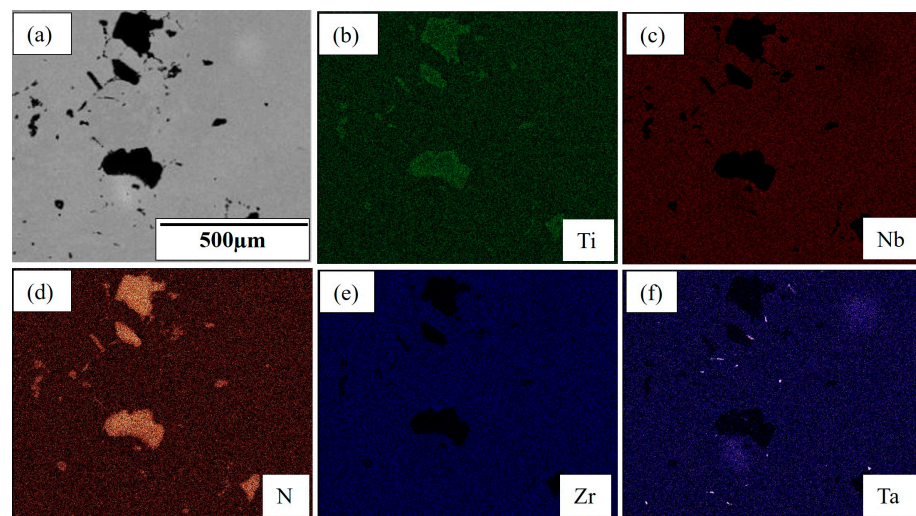
Figure 4. (**a**) SEM image of the TNZT-2 wt.% TiN composite with the corresponding EDS maps of (**b**) Ti, (**c**) Nb, (**d**) N, (**e**) Zr, and (**f**) Ta.

3.3. Microhardness

The microhardness results for the SPS-processed pure TNZT alloys and TNZT composites with 2 wt.% ZrN, TaN, NbN, and TiN are shown in Figure 5a. The pure TNZT alloy demonstrated the lowest average hardness of 183.1 HV. The average hardness of the TNZT composites with 2 wt.% ZrN, TaN, and NbN was 281.4, 288.1, and 292 HV, respectively. This showed that the addition of ZrN improved the hardness by ~53%, the addition of TaN improved the hardness by ~57%, and the addition of NbN improved the hardness by ~59%. TNZT composites reinforced with 2 wt.% TiN showed the maximum average hardness of 311.8 HV, enhancing the hardness of TNZT alloys by ~70%. The addition of nitrides leads to grain refinement, resulting in an increase in hardness, which can be expressed by using the Hall–Petch equation shown in Equation (1) [45]:

$$H_V = H_0 + kd^{-1/2} \tag{1}$$

where H_V is the hardness of the composite, d is the grain size, and H_0 and k are the empirical constants. As the hardness of the composite is inversely proportional to the square root of the grain size, a decreasing grain size contributes to an increase in hardness. An increase in the number of grain boundaries in small grains compared to coarse grains effectively restricts the movement of dislocation, which is responsible for a lower plastic deformation during indentation loading and contributes to a higher hardness. All nitride-reinforced TNZT composites followed the trend that an increase in hardness corresponds to a decrease in grain size. A greater hardness value for the TNZT–NbN composite can be attributed to the higher hardness of NbN, which effectively inhibits matrix movement near NbN particles during loading. The microhardness results are in agreement with the SEM results and EDS analysis which showed the distribution of nitrides in nitride-reinforced TNZT composites cause an enhanced hardness and associated mechanical properties.
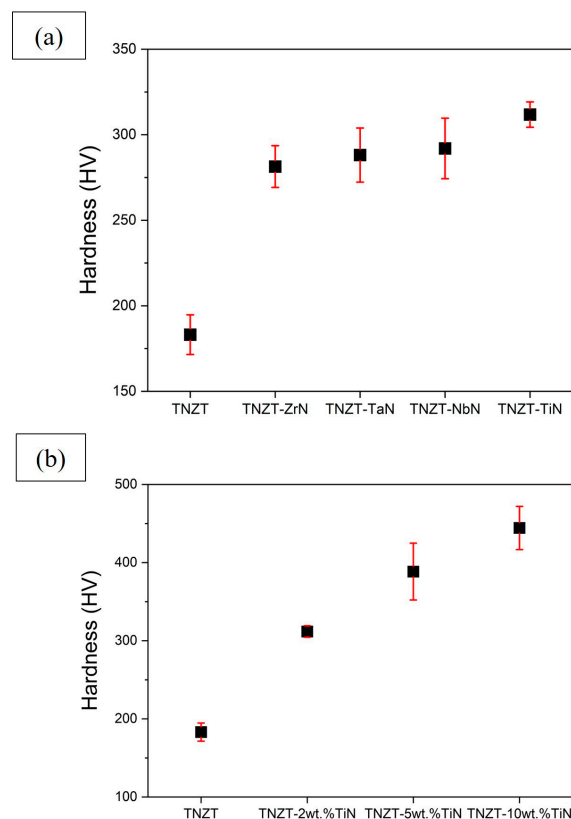

Figure 5. (**a**) Variation in the hardness of sintered TNZT composites with (**a**) 2 wt.% ZrN, TaN, NbN, and TiN, and (**b**) 2 wt.%, 5 wt.%, and 10 wt.% TiN. The results shown are the mean ± standard deviation.

The effect of increasing the TiN content on the microhardness of sintered TNZT composites is shown in Figure 5b. It can be observed that the average hardness values increase with a higher incorporation of TiN. TNZT-5 wt.% TiN showed an average hardness of 388.5 HV, improving the hardness of TNZT alloys by ~112%. TNZT-10 wt.% TiN showed an average hardness of 444.3 HV, improving the hardness of TNZT alloys by ~143%. An increase in TiN reinforcement leads to a decrease in the grain-size increase in hardness values.

The relatively inhomogeneous distributions of TiN may have caused a drastic improvement in the hardness of TNZT-10 wt.% TiN composites.

3.4. Wear Behavior

Wear experiments were performed to compare the tribological performance of nitride-reinforced TNZT composites with pure TNZT alloys and to understand two relevant tribological phenomena: friction and wear. These phenomena help in predicting the extent of deterioration in materials and the dissipation of energy. Friction is associated with the force that opposes or restricts the relative sliding motion between two solid surfaces. Wear represents the loss of material from one or both mating solid surfaces. The understanding of the friction and wear of TNZT composites is crucial for making orthopedic implants that are subjected to continuous friction. Coefficient of friction (CoF) measurements and wear track analysis are the quantitative assessments used to understand the tribological behavior of various materials. CoF is the ratio between the force of friction (F) acting on two bodies and the normal force (P) that presses them together.

The sliding wear behavior for all sintered TNZT composites with sliding distance Is shown in Figure 6. Figure 6a compares the CoF of different nitride TNZT composites with the pure TNZT alloy, whereas Figure 6b shows the effect of TiN addition on the CoF of TNZT composites. The reported result for the tribology test reflects that the pure TNZT sample has the highest CoF, equal to 0.823, compared to all nitride-reinforced TNZT composites. The average CoF of the TNZT composites with 2 wt.% ZrN, TaN, and NbN was 0.774, 0.752, and 0.739, respectively. Among all the reinforcing nitrides, the addition of 2 wt.% TiN in TNZT composites achieved the highest reduction in CoF compared to the pure TNZT matrix. The addition of 2 wt.% TiN in TNZT reduced the 0.823 CoF of pure TNZT to 0.659. CoF plots exhibited a fluctuating trend for the 2 wt.% TiN–TNZT composite with an insignificant fluctuation in CoF from 0.6 to 0.7 mainly due to the waviness of the specimen. A similar fluctuation trend was observed in previous research results from waviness [46]. As TNZT is softer and less abrasive, its surface undergoes a plastic shear deformation during wear loading resulting in the smearing and ductile stacking of coarse wear platelets aligned along the sliding direction [38]. Long and Rack also explained the excessive plastic deformation, including significant surface depressions with material removal, prows of smeared metal, micro-cracking, and micro-plowing as potential wear mechanisms for the pure TNZT during wear testing [47]. A higher hardness leads to a lower wear volume, resulting in a lower CoF governed by Archard Law. The variation in CoF with a different nitride incorporation is in accordance with a variation in hardness. An improved hardness reduces the true contact area between the nitrided composites and the Si_3N_4 counterface, leading to lower wear and hence a lower CoF. The ability of nitrides to increase the tribological performance of TNZT alloys by reducing the CoF presented the following trend: TiN > NbN > TaN > ZrN. In the case of the TiN–TNZT composite, along with hardness, the creation of more stable shear bands formed due to strain-induced plastic deformation showed the capacity to bear the interfacial shear stresses during sliding contact, resulting in minimized wear [38].
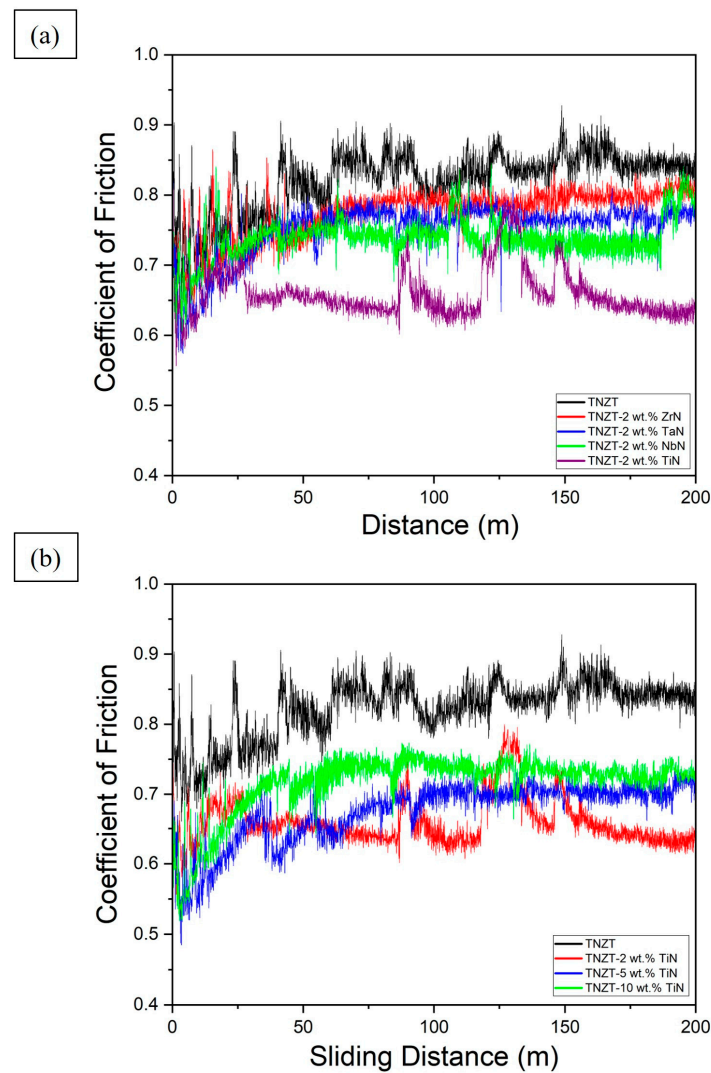
Figure 6. Variation in the CoF with sliding distance for sintered TNZT composites with (**a**) 2 wt.% ZrN, TaN, NbN, and TiN, and (**b**) 2 wt.%, 5 wt.%, and 10 wt.% TiN.

The average CoF of TNZT composites with 5 wt.% TiN and 10 wt.% TiN was 0.674 and 0.715, respectively. This increase in CoF with a higher amount of TiN addition is attributed to the nonhomogeneous distribution of TiN reinforcements, which leads to a higher wear and material deterioration. The SEM wear track images and EDS maps for TNZT-2 wt.% TiN and TNZT-10 wt.% TiN composites after wear testing are shown in Figures 7 and 8, respectively. The coarse wear debris along the moving direction was observed over the wear track. For the TNZT-2 wt.% TiN composite, less wear debris compared to TNZT-10 wt.% TiN was observed in the SEM micrographs, which is in good agreement with the CoF plots represented in Figure 6b. The ductile stacking and irregular elongated course layer plates with microcracks in the SEM images confirm that plastic shear deformation can be a potential wear mechanism for the TNZT–TiN composite. The nonhomogenous distribution of hard and brittle TiN in TNZT-10 wt.% TiN gives short wear debris over the wear surface, indicating a three-body abrasive wear mechanism. Three-body wear is the result of loose particles from the brittle surface freely rolling, sliding, and scraping the soft surface. This further inflicts damage and causes high wear volume [48]. Wear track EDS mapping shows the presence of no element other than Ti, N, Nb, Zr, and Ta, which suggests TiN reinforcement is primarily responsible for the improved wear volume and lower CoF in TNZT–TiN compared to other nitrides. This can be observed and confirmed with the EDS

maps shown in Figures 7 and 8 for TNZT-2 wt.% TiN and TNZT-10 wt.% TiN, respectively, where the latter showed a higher wear and more material loss in wear tracks.
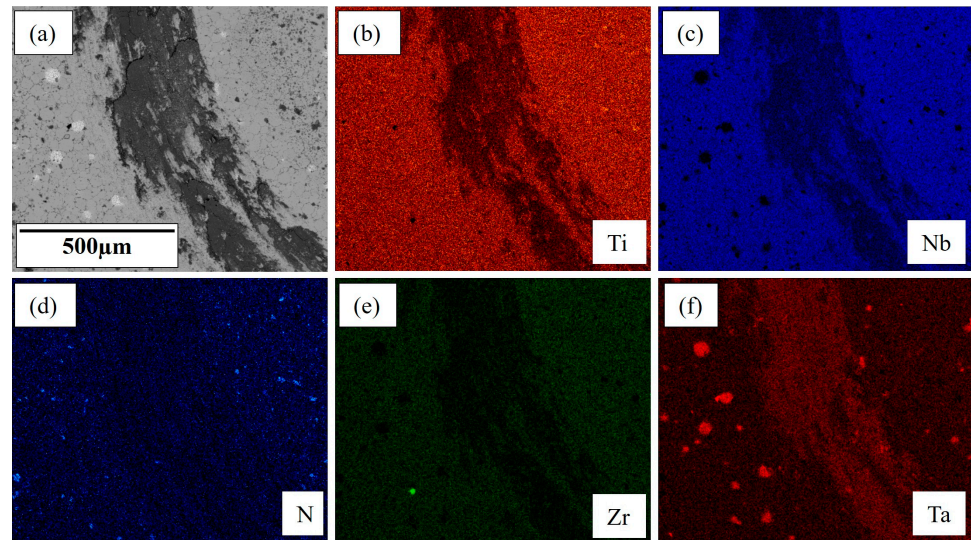

Figure 7. (**a**) SEM image of sintered the TNZT-2 wt.% TiN composite with the corresponding EDS maps of (**b**) Ti, (**c**) Nb, (**d**) N, (**e**) Zr, and (**f**) Ta.
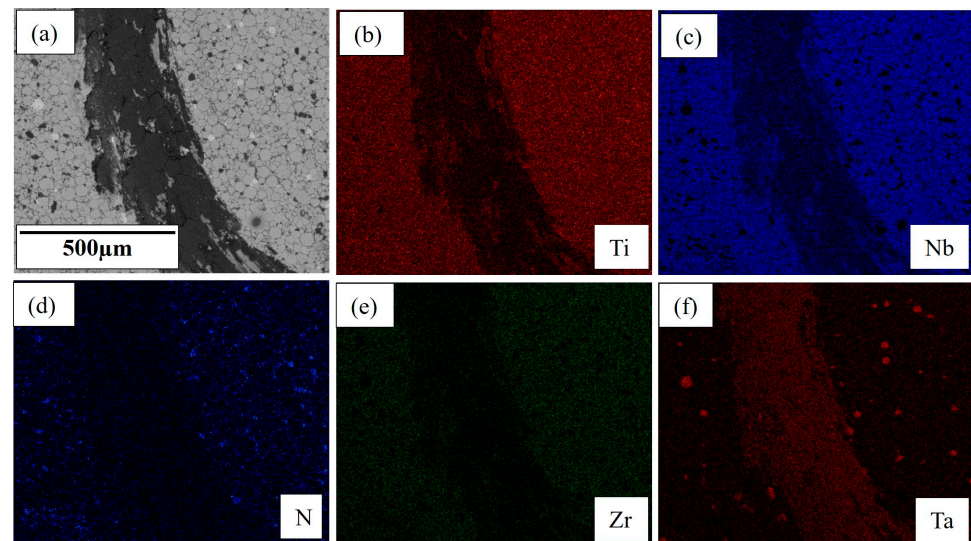

Figure 8. (**a**) SEM image of sintered the TNZT-10 wt.% TiN composite with the corresponding EDS maps of (**b**) Ti, (**c**) Nb, (**d**) N, (**e**) Zr, and (**f**) Ta.

3.5. Cytotoxicity Studies

Cell viability was tested using cytotoxicity staining protocols after culturing cells in incubators for 48 h at 37 °C and 5% CO_2 on four different alloy surfaces (*n* = 4 wells/ alloy type). The images were obtained using an inverted fluorescence microscope. The green stain represents live cells, while the red stain represents dead cells in these cultures. Representative images (Figure 9) suggest that there are very few dead cells in all four cases, suggesting there was no perceivable acute toxicity of the alloys on MG-63 cells. Quantitative analysis suggested that cell survival was similar to that noted in control cultures (Figure 10).
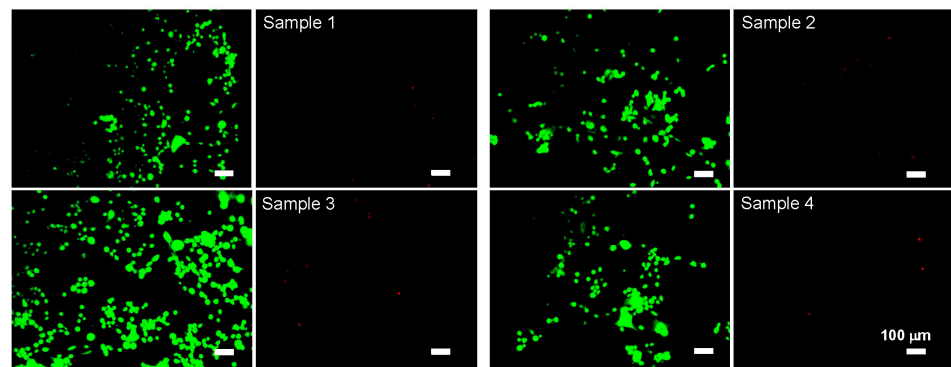
Figure 9. Representative stained fluorescence images obtained in green and red channels after 48 h of culture on four different types of alloy samples. Scale bar: 100 μm. Sample 1 (TNZT-2 wt.% ZrN), Sample 2 (TNZT-2 wt.% TaN), Sample 3 (TNZT-2 wt.% TiN), and Sample 4 (TNZT-2 wt.% NbN).
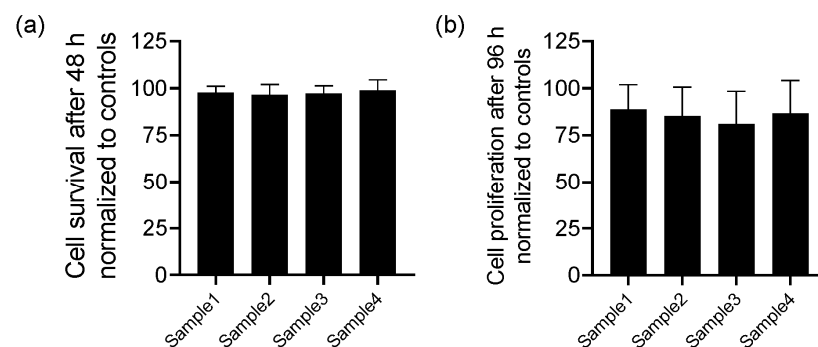

Figure 10. Quantification of MG-63 cell viability on alloy samples for (**a**) 48 h and (**b**) 96 h. No discernible difference was noted between the control cultures and the cultures on alloy samples, suggesting that the metals are not acutely toxic to these cells. The results shown are the mean $\pm$ standard error. Sample 1 (TNZT-2 wt.% ZrN), Sample 2 (TNZT-2 wt.% TaN), Sample 3 (TNZT-2 wt.% TiN), and Sample 4 (TNZT-2 wt.% NbN).

The results from the MTT assay (Figure 10) showed no significant differences in cell proliferation between the control cultures (cells cultured on a plastic surface) and the cultures on alloy surfaces over the 96 h duration.

MG-63 cells seeded on the surfaces of various alloys were imaged using a Wilson VH1202 Micro Hardness Tester microscope, using a 10× objective. Representative images (Figure 11) show cell attachment and proliferation on the surface of alloy surfaces. A spindle-shaped cell morphology was noted in all the cases similar to those in the controls. The microscale imperfections on the alloy surfaces are common for such specimens.

A cytotoxicity analysis was performed for the four different metal alloy compositions. An MG-63 osteoblast-like cell line was used as a model cell for this study, and its survival, proliferation, and attachment to these alloy surfaces were assessed. Osteogenic sarcoma cells (e.g., MG-63 cell line) are ideal for evaluating the cytotoxicity of such alloys, as they proliferate and rapidly grow while still maintaining a sensitivity to variations in their microenvironment. The results from the cytotoxicity test and MTT assay suggest no acute toxicity emanating from these alloys compared to that in control cultures. Despite differences in the composition of each ingredient in these TNZT alloys, osteoblasts [49,50] or fibroblasts [51,52] cultured on TNZT surfaces showed no noticeable compromise in cell viability even at chronic time points (>180 days in culture). This could perhaps be due to an excellent corrosion resistance and the nontoxicity of the elements in these alloys in cell culture media.
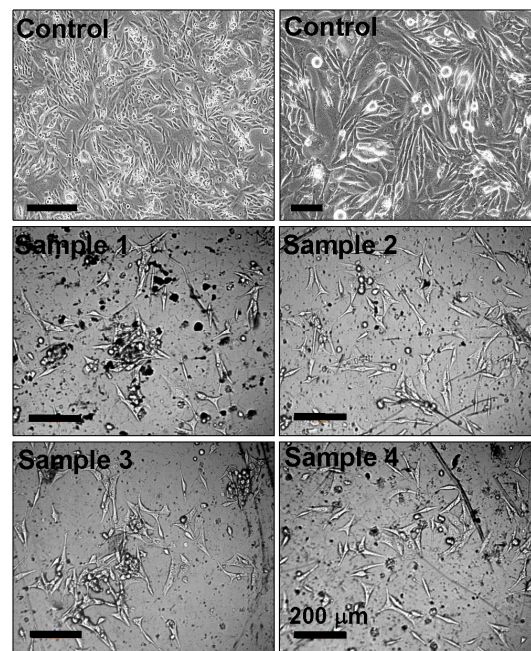
Figure 11. Representative images of cell adhesion on the surfaces of various metal alloys. Scale bar: 200 μm. Sample 1 (TNZT-2 wt.% ZrN), Sample 2 (TNZT-2 wt.% TaN), Sample 3 (TNZT-2 wt.% TiN), and Sample 4 (TNZT-2 wt.% NbN). Controls represent cultures on 2D tissue culture plastic dishes.

The results are in broad agreement with similar reports on the biocompatibility of TNZT alloys. For instance, human dental pulp stem cells and MG-63 cells have exhibited excellent viability, adhesion, proliferation, and differentiation, with no conceivable cytotoxicity when cultured in the presence of as-cast Ti–35Nb–7Zr–5Ta alloys [53]. Similarly, TNZT alloys of a similar composition and prepared via laser powder bed fusion showed excellent in vitro cytocompatibility (survival, adhesion, proliferation) when MC3T3-E1 cells were cultured on their surfaces and the addition of silicon of up to 5% did not alter such biocompatibility properties [54]. In yet another study, L929 cells (mouse fibroblast cell line) cultured on Ti–30Nb–5Ta–3Zr alloys manufactured by a powder-based selective laser melting process adhered well to the surface and proliferated similar to those in controls [51]. In general, the biocompatibility of these alloys appears to be independent of their microstructural features (porosity, pore size, surface roughness), chemical composition, and mechanical characteristics and seem to arise from low-stress shielding and the nontoxic and nonallergenic nature of the compounds in the alloy.

4. Conclusions

The effect of various nitride (TiN, NbN, ZrN, and TaN) reinforcement on the mechanical, tribological, and biological properties of β-Ti (TNZT) alloys was studied using XRD, SEM/EDS, microhardness testing, and wear testing.

- All nitride-reinforced TNZT composites demonstrated superior tribological performance over pure TNZT alloys while retaining a single-phase BCC structure and excellent biocompatibility. This was attributed to the presence of very hard and strong nitrides in the β-Ti matrix.
- TNZT-2 wt.% TiN exhibited the optimum hardness (311.8 HV) and lowest CoF (0.659), showcasing the highest efficiency of TiN among other nitrides in improving the tribological performance of TNZT alloys.
- TNZT composites with 5 wt.% TiN and 10 wt.% TiN showed a higher hardness (388.5 HV and 444.3 HV, respectively) but also showed a higher CoF (0.674 and 0.715, respectively). This was attributed to the higher but nonuniform presence of TiN.

- This work will aid in producing superior β-Ti alloys for advanced orthopedic applications.

References

1. Scholz, M.S.; Blanchfield, J.P.; Bloom, L.D.; Coburn, B.H.; Elkington, M.; Fuller, J.D.; Bond, I.P. The use of composite materials in modern orthopedic medicine and prosthetic devices: A review. *Compos. Sci. Technol.* **2011**, *71*, 1791–1803. [CrossRef]
2. Filip, N.; Radu, I.; Veliceasa, B.; Filip, C.; Pertea, M.; Clim, A.; Pinzariu, A.C.; Drochioi, L.C.; Hilitanu, R.L.; Serban, I.L. Biomaterials in Orthopedic Devices: Current Issues and Future Perspectives. *Coatings* **2022**, *12*, 1544. [CrossRef]
3. Intravaia, J.T.; Graham, T.; Kim, H.S.; Nanda, H.S.; Kumbar, S.G.; Nukavarapu, S.P. Smart orthopedic biomaterials and implants. *Curr. Opin. Biomed. Eng.* **2023**, *25*, 100439. [CrossRef] [PubMed]
4. Choi, S.R.; Kwon, J.W.; Suk, K.S.; Kim, H.S.; Moon, S.H.; Park, S.Y.; Lee, B.H. The Clinical Use of Osteobiologic and Metallic Biomaterials in Orthopedic Surgery: The Present and the Future. *Materials* **2023**, *16*, 3633. [CrossRef]
5. Liang, W.; Zhou, C.; Zhang, H.; Bai, J.; Jiang, B.; Jiang, C.; Ming, W.; Zhang, H.; Long, H.; Huang, X.; et al. Recent advances in 3D printing of biodegradable metals for orthopaedic applications. *J. Biol. Eng.* **2023**, *17*, 56. [CrossRef] [PubMed]
6. Affatato, S.; Ruggiero, A.; Merola, M. Advanced biomaterials in hip joint arthroplasty. A review on polymer and ceramics composites as alternative bearings. *Compos. B Eng.* **2015**, *83*, 276–283. [CrossRef]
7. Niinomi, M.; Nakai, M.; Hieda, J. Development of new metallic alloys for biomedical applications. *Acta Biomater.* **2012**, *8*, 3888–3903. [CrossRef] [PubMed]
8. Prakasam, M.; Locs, J.; Salma-Ancane, K.; Loca, D.; Largeteau, A.; Berzina-Cimdina, L. Biodegradable materials and metallic implants—A review. *J. Funct. Biomater.* **2017**, *8*, 44. [CrossRef]
9. Kulkarni, M.; Mazare, A.; Gongadze, E.; Perutkova, Š.; Kralj-Iglič, V.; Milošev, I.; Schmuki, P.; Iglič, A.; Mozetič, M. Titanium nanostructures for biomedical applications. *Nanotechnology* **2015**, *26*, 062002. [CrossRef]
10. Minagar, S.; Berndt, C.C.; Wang, J.; Ivanova, E.; Wen, C. A review of the application of anodization for the fabrication of nanotubes on metal implant surfaces. *Acta Biomater.* **2012**, *8*, 2875–2888. [CrossRef]
11. Amaravathy, P.; Sowndarya, S.; Sathyanarayanan, S.; Rajendran, N. Novel sol gel coating of Nb_2O_5 on magnesium alloy for biomedical applications. *Surf. Coat. Technol.* **2014**, *244*, 131–141. [CrossRef]
12. Mazur, M.; Kalisz, M.; Wojcieszak, D.; Grobelny, M.; Mazur, P.; Kaczmarek, D.; Domaradzki, J. Determination of structural, mechanical and corrosion properties of Nb_2O_5 and $(Nb_yCu_{1-y})O_x$ thin films deposited on Ti6Al4V alloy substrates for dental implant applications. *Mater. Sci. Eng. C* **2015**, *47*, 211–221. [CrossRef]
13. Li, Q.; Liu, T.; Li, J.; Cheng, C.; Niinomi, M.; Yamanaka, K.; Chiba, A.; Nakano, T. Microstructure, mechanical properties, and cytotoxicity of low Young's modulus Ti–Nb–Fe–Sn alloys. *J. Mater. Sci.* **2022**, *57*, 5634–5644. [CrossRef]
14. Bahl, S.; Suwas, S.; Chatterjee, K. Comprehensive review on alloy design, processing, and performance of β Titanium alloys as biomedical materials. *Int. Mater. Rev.* **2021**, *66*, 114–139. [CrossRef]
15. Song, X.; Wang, L.; Niinomi, M.; Nakai, M.; Liu, Y. Fatigue characteristics of a biomedical β-type titanium alloy with titanium boride. *Mater. Sci. Eng. A* **2015**, *640*, 154–164. [CrossRef]
16. Chirico, C.; Romero, A.V.; Gordo, E.; Tsipas, S.A. Improvement of wear resistance of low-cost powder metallurgy β-titanium alloys for biomedical applications. *Surf. Coat. Technol.* **2022**, *434*, 128207. [CrossRef]
17. Biesiekierski, A.; Ping, D.; Li, Y.; Lin, J.; Munir, K.S.; Yamabe-Mitarai, Y.; Wen, C. Extraordinary high strength Ti-Zr-Ta alloys through nanoscaled, dual-cubic spinodal reinforcement. *Acta Biomater.* **2017**, *53*, 549–558. [CrossRef]
18. Maity, T.; Balcı, Ö.; Gammer, C.; Ivanov, E.; Eckert, J.; Prashanth, K.G. High pressure torsion induced lowering of Young's modulus in high strength TNZT alloy for bio-implant applications. *J. Mech. Behav. Biomed. Mater.* **2020**, *108*, 103839. [CrossRef]
19. Liu, J.; Chang, L.; Liu, H.; Li, Y.; Yang, H.; Ruan, J. Microstructure, mechanical behavior and biocompatibility of powder metallurgy Nb-Ti-Ta alloys as biomedical material. *Mater. Sci. Eng. C* **2017**, *71*, 512–519. [CrossRef]
20. Morais, L.S.; Serra, G.G.; Muller, C.A.; Andrade, L.R.; Palermo, E.F.; Elias, C.N.; Meyers, M. Titanium alloy mini-implants for orthodontic anchorage: Immediate loading and metal ion release. *Acta Biomater.* **2007**, *3*, 331–339. [CrossRef]
21. Li, H.F.; Huang, J.Y.; Lin, G.C.; Wang, P.Y. Recent advances in tribological and wear properties of biomedical metallic materials. *Rare Met.* **2021**, *40*, 3091–3106. [CrossRef]

22. Marin, E.; Lanzutti, A. Biomedical Applications of Titanium Alloys: A Comprehensive Review. *Materials* **2024**, *17*, 114. [CrossRef]
23. Li, C.; Zhan, Y.; Jiang, W. β-Type Ti–Mo–Si ternary alloys designed for biomedical applications. *Mater. Des.* **2012**, *34*, 479–482. [CrossRef]
24. Taddei, E.B.; Henriques, V.A.R.; Silva, C.R.M.; Cairo, C.A.A. Production of new titanium alloy for orthopedic implants. *Mater. Sci. Eng. C* **2004**, *24*, 683–687. [CrossRef]
25. Hager Jr, C.H.; Sanders, J.; Sharma, S.; Voevodin, A. Gross slip fretting wear of CrCN, TiAlN, Ni, and CuNiIn coatings on Ti6Al4V interfaces. *Wear* **2007**, *263*, 430–443. [CrossRef]
26. Gupta, M.K.; Etri, H.E.; Korkmaz, M.E.; Ross, N.S.; Krolczyk, G.M.; Gawlik, J.; Yasar, N.; Pimenov, D.Y. Tribological and surface morphological characteristics of titanium alloys: A review. *Arch. Civ. Mech. Eng.* **2022**, *22*, 72. [CrossRef]
27. Samuel, S.; Nag, S.; Scharf, T.W.; Banerjee, R. Wear resistance of laser-deposited boride reinforced Ti-Nb–Zr–Ta alloy composites for orthopedic implants. *Mater. Sci. Eng. C* **2008**, *28*, 414–420. [CrossRef]
28. Chan, C.W.; Lee, S.; Smith, G.; Sarri, G.; Ng, C.H.; Sharba, A.; Man, H.C. Enhancement of wear and corrosion resistance of beta titanium alloy by laser gas alloying with nitrogen. *Appl. Surf. Sci.* **2016**, *367*, 80–90. [CrossRef]
29. Geetha, M.; Singh, A.K.; Asokamani, R.; Gogia, A.K. Ti based biomaterials, the ultimate choice for orthopaedic implants—A review. *Prog. Mater. Sci.* **2009**, *54*, 397–425. [CrossRef]
30. Raveh, A.; Hansen, P.L.; Avni, R.; Grill, A. Microstructure and composition of plasma-nitrided Ti-6Al-4V layers. *Surf. Coat. Technol.* **1989**, *38*, 339–351. [CrossRef]
31. Matsuura, K.; Kudoh, M. Surface modification of titanium by a diffusional carbo-nitriding method. *Acta Mater.* **2002**, *50*, 2693–2700. [CrossRef]
32. Sathish, S.; Geetha, M.; Pandey, N.D.; Richard, C.; Asokamani, R. Studies on the corrosion and wear behavior of the laser nitrided biomedical titanium and its alloys. *Mater. Sci. Eng. C* **2010**, *30*, 376–382. [CrossRef]
33. Cui, Z.D.; Zhu, S.L.; Man, H.C.; Yang, X.J. Microstructure and wear performance of gradient Ti/TiN metal matrix composite coating synthesized using a gas nitriding technology. *Surf. Coat. Technol.* **2005**, *190*, 309–313. [CrossRef]
34. Borkar, T.; Nag, S.; Ren, Y.; Tiley, J.; Banerjee, R. Reactive spark plasma sintering (SPS) of nitride reinforced titanium alloy composites. *J. Alloys Compd.* **2014**, *617*, 933–945. [CrossRef]
35. Tjong, S.C.; Ma, Z.Y. Microstructural and mechanical characteristics of in situ metal matrix composites. *Mater. Sci. Eng. R Rep.* **2000**, *29*, 49–113. [CrossRef]
36. Ma, Z.Y.; Ning, X.G.; Lu, Y.X.; Bi, J.; Wen, L.S.; Wu, S.J.; Jangg, G.; Daninger, H. In-situ Al$_4$C$_3$ dispersoid and SiC particle mixture-reinforced aluminium composite. *Scr. Met. Mater.* **1994**, *31*, 131–135. [CrossRef]
37. Attar, H.; Ehtemam-Haghighi, S.; Kent, D.; Dargusch, M.S. Recent developments and opportunities in additive manufacturing of titanium-based matrix composites: A review. *Int. J. Mach. Tools Manuf.* **2018**, *133*, 85–102. [CrossRef]
38. Mohseni, H.; Nandwana, P.; Tsoi, A.; Banerjee, R.; Scharf, T.W. In situ nitrided titanium alloys: Microstructural evolution during solidification and wear. *Acta Mater.* **2015**, *83*, 61–74. [CrossRef]
39. Benjamin, J.S.; Volin, T.E. The mechanism of mechanical alloying. *Metall. Trans.* **1974**, *5*, 1929–1934. [CrossRef]
40. Gilman, P.S.; Benjamin, J.S. Mechanical alloying. *Annu. Rev. Mater. Sci.* **1983**, *13*, 279–300. [CrossRef]
41. Zhou, D.; Qiu, F.; Wang, H.; Jiang, Q. Manufacture of nano-sized particle-reinforced metal matrix composites: A review. *Acta Metall. Sin-Engl.* **2014**, *27*, 798–805. [CrossRef]
42. Mamedov, V. Spark plasma sintering as advanced PM sintering method. *Powder Metall.* **2002**, *45*, 322–328. [CrossRef]
43. Walunj, G.; Desai, J.; Bohara, S.; Contieri, R.; Kothapalli, C.; Ivanov, E.; Borkar, T. Light Weight-Low Modulus Biocompatible Titanium Alloys Processed via Spark Plasma Sintering. *J. Alloys Metall. Syst.* **2023**, *3*, 100018. [CrossRef]
44. Batalha, R.L.; Batalha, R.L.; Pinotti, V.E.; Pinotti, V.E.; Alnoaimy, O.O.S.; Alnoaimy, O.O.S.; Batalha, W.C.; Batalha, W.C.; Gustmann, T.; Gustmann, T.; et al. Microstructure and properties of TiB$_2$-reinforced Ti–35Nb–7Zr–5Ta processed by laser-powder bed fusion. *J. Mater. Res.* **2022**, *37*, 259–271. [CrossRef]
45. Facchini, D. Biomedical nanocrystalline metals and alloys: Structure, properties and applications. In *Nanomedicine*; Woodhead Publishing: Sawston, UK, 2012; pp. 36–67. [CrossRef]
46. Li, Y.; Garabedian, N.; Schneider, J.; Greiner, C. Waviness affects friction and abrasive wear. *Tribol. Lett.* **2023**, *71*, 64. [CrossRef]
47. Long, M.; Rack, H.J. Friction and surface behavior of selected titanium alloys during reciprocating-sliding motion. *Wear* **2001**, *249*, 157–167. [CrossRef]
48. Li, Y.; Schreiber, P.; Schneider, J.; Greiner, C. Tribological mechanisms of slurry abrasive wear. *Friction* **2023**, *11*, 1079–1093. [CrossRef]
49. Carreño, G.; Pereira, A.; Ávila-Salas, F.; Marican, A.; Andrade, F.; Roca-Melendres, M.M.; Valdes, O.; Vijayakumar, S.; Schwartz, S., Jr.; Abasolo, I.; et al. Development of "on-demand" thermo-responsive hydrogels for anti-cancer drugs sustained release: Rational design, in silico prediction and in vitro validation in colon cancer models. *Mater. Sci. Eng. C* **2021**, *131*, 112483. [CrossRef]
50. Niinomi, M. Design and development of metallic biomaterials with biological and mechanical biocompatibility. *J. Biomed. Mater. Res. A* **2019**, *107*, 944–954. [CrossRef]
51. Luo, J.P.; Sun, J.F.; Huang, Y.J.; Zhang, J.H.; Zhang, Y.D.; Zhao, D.P.; Yan, M. Low-modulus biomedical Ti–30Nb–5Ta–3Zr additively manufactured by Selective Laser Melting and its biocompatibility. *Mater. Sci. Eng. C* **2019**, *97*, 275–284. [CrossRef]

52. Luo, J.P.; Huang, Y.J.; Xu, J.Y.; Sun, J.F.; Dargusch, M.S.; Hou, C.H.; Ren, L.; Wang, R.Z.; Ebel, T.; Yan, M. Additively manufactured biomedical Ti-Nb-Ta-Zr lattices with tunable Young's modulus: Mechanical property, biocompatibility, and proteomics analysis. *Mater. Sci. Eng. C* **2020**, *114*, 110903. [CrossRef] [PubMed]

53. Rossi, M.C.; Ventura, B.N.; Milián, L.; Escuder, A.V.; Amigó Borrás, V. Study of Electrochemical and Biological Characteristics of As-Cast Ti-Nb-Zr-Ta System Based on Its Microstructure. *Metals* **2022**, *12*, 476. [CrossRef]

54. Luo, X.; Yang, C.; Li, R.Y.; Wang, H.; Lu, H.Z.; Song, T.; Ma, H.W.; Li, D.D.; Gebert, A.; Li, Y.Y. Effect of silicon content on the microstructure evolution, mechanical properties, and biocompatibility of β-type TiNbZrTa alloys fabricated by laser powder bed fusion. *Biomater. Adv.* **2022**, *133*, 112625. [CrossRef] [PubMed]